# Trikafta rescues F508del-CFTR by tightening specific phosphorylation-dependent interdomain interactions

Short title: Correction pathway of ΔF508-CFTR

Guangyu Wang[1,2]*

[1]Department of Physiology and Membrane Biology, University of California School of Medicine, Davis, CA, USA

[2]Department of Drug Research and Development, Institute of Biophysical Medico-chemistry, Reno, NV, USA

* Correspondence E-mail: gary.wang10@gmail.com

American Heart Association: 10SDG4120011

**Abstract**

Trikafta is well-known for correcting thermal and gating defects caused by the most common cystic fibrosis mutation F508del in the human cystic fibrosis transmembrane conductance regulator even at a physiological temperature. However, the exact correction pathway is still unclear. Here, noncovalent interactions among two transmembrane domains (TMD1 and TMD2), the regulatory (R) domain and two nucleotide binding domains (NBD1 and NBD2) were analyzed. The thermal stability of NBD1 was also evaluated through its tertiary constrained noncovalent interaction networks or thermoring structures. The results demonstrated that Trikafta binding to flexible TMD1 and TMD2 rearranged their interactions with the R domain upon phosphorylation, coupling tightened cytoplasmic TMD1-TMD2 interactions to tightened Mg/ATP-dependent NBD1-NBD2 dimerization, which stabilized NBD1 above human body temperature. Overall, although the deletion of F508 induces the primary thermal defect in NBD1 and then the gating defect at the TMD1-TMD2 interface, Trikafta rescued them in a reverse manner

allosterically. These mechanistic insights into the precise correction pathway of this misfolded channel facilitate optimizing cystic fibrosis treatment. (165 words)

**Key words:** allosteric pathway, digital biology, grid thermodynamic signature, least-stable interaction, melting threshold, noncovalent thermoring structure, partial unfolding, protein stability

Key points

- Trikafta binding to flexible TMD1 and TMD2 tightened their cytoplasmic interactions.
- Tight cytoplasmic TMD1-TMD2 interactions primed the specific binding of the dynamic phosphorylated S813 site to the TMD1/TMD2/NBD1 interfaces.
- The tight binding of the S813 site to the TMD1/TMD2/NBD1 interfaces strengthened NBD1-NBD2 dimerization which stabilizes NBD1.

## INTRODUCTION

Cystic fibrosis (CF) is the most common fatal genetic disease in the Caucasian population and is also prevalent in other human populations. On the other hand, secretory diarrhea is the leading cause of infant mortality worldwide. A key issue in both of these devastating diseases is a protein called Cystic Fibrosis Transmembrane conductance Regulator (CFTR) with activity that is either too low or too high. CFTR belongs to the family of ATP-binding cassette (ABC) transporters but functions as a phosphorylation-dependent and ATP-gated anion (chloride or bicarbonate) channel. It regulates the salt-water balance of the lung, intestine, pancreas, and sweat once expressed on the cell plasma membrane in epithelial tissues around the human body (1-4). To date, more than 2000 mutations in CFTR have been found to cause CF (http://www.genet.sickkids.on.ca/cftr; CFTR2 database: https://cftr2.org). The most common mutation (70 % of CF cases) is ΔF508, which has both gating and thermal defects, leading to airway bacterial infection and respiratory failure (4-13).

A cryo-electron microscopy (cryo-EM) structure of dephosphorylated human CFTR (PDB, 5UAK) reveals that it starts with a lasso motif (1-37) and is composed of five well-known domains in the following order: transmembrane domain 1 (TMD1) (38-383), nucleotide binding domain 1 (NBD1) (384-645), the regulatory (R) domain (646-843), transmembrane domain 2 (TMD2) (844-1172), and nucleotide binding domain 2 (NBD2) (1173-1436). Both TMD1 and TMD2 line an anion conduction pathway, each consisting of six transmembrane (TM) helices that extend to the intracellular loops (ICLs). The arrangement of TM1, 2, 3 and 6 forming a bundle with TM10 and 11, while the remaining TM helices build another bundle, allows for domain swapping. This enables NBD1 to primarily connect with TMD2 via ICL4 and NBD2 to mainly relate to TMD1 via ICL2 (14). When the R domain is phosphorylated by protein kinase A (PKA) for Mg/ATP-mediated NBD1-NBD2 dimerization, the hydrolysis-deficient E1371Q mutant is open with distinct NBD1-ICL4 and NBD2-ICL2 interactions (15, 16).

In contrast, the most common cystic fibrosis-causing ΔF508 mutant primarily destabilizes NBD1 and nearby interdomain interactions (17-21). Even if a type I corrector like lumacaftor (VX-809) is bound to TMD1 in the phosphorylated and ATP-bound conformation to secure the channel expression on the cell surface, NBD1 folding remains flexible, resembling a "molten globule" until the folding corrector tezacaftor (VX-661), the folding and gating modulator elexacaftor (VX-445) and the channel activity potentiator ivacaftor (VX-770) are combined in

Trikafta (branded as Kaftrio in Europe) and bound to TMD1 and TMD2. This combination therapy completely restores ΔF508 to an NBD-dimerized conformation with ATP fully occluded at both the consensus and degenerate sites (22). Although Trikafta synergistically rescued the gating and thermal defects of ΔF508-CFTR at 37 °C (23-27), much less is known about the exact correction pathway of the most flexible NBD1.

On the other hand, while the thermostability of isolated hNBD1 can be measured using differential scanning calorimetry (DSC) or differential scanning fluorimetry (DSF) (9,11, 28-29), directly measuring NBD1's thermostability with either biophysical approach becomes impossible in the presence of various interdomain interactions when it is not isolated from the full-length hCFTR. Therefore, an alternative tool is necessary to assess the effects of adjacent interdomain interactions on NBD1's thermostability and to unveil the rescue pathway of the thermal defect of ΔF508 CFTR by Trikafta even within such a complex multi-domain protein.

Recently, a novel and highly sensitive graphical method has been developed to analyze the structural thermo-stability and predict activity temperatures of proteins including enzymes (30-37). Based on their high-resolution 3D structures, the tertiary noncovalent interaction networks can be constrained by a grid thermodynamic model as the thermoring structures to stabilize each interaction along the single polypeptide. Each thermoring is denoted as $Grid_s$, where "$_s$" is the grid size to regulate the intensity of the least-stable noncovalent interaction within this grid. It can be defined by the shortest alternative path or the minimal free amino acid side chains to link two ends of this least-stable interaction along the single polypeptide chain and other noncovalent interactions. When the biggest thermoring is identified, the melting temperature threshold ($T_{m,th}$) to unfold the least-stable noncovalent interaction within the biggest thermoring along the single polypeptide can be calculated. Both theoretical and experimental $T_{m,th}$ values matched well for isolated human NBD1 (hNBD1) upon different structural perturbations (37), allowing this graphical analysis to be extended to predict the $T_{m,th}$ values of NBD1 and evaluate the effects of the interdomain interactions on NBD1's thermostability within the full-length hCFTR. In addition, the systematic thermal instability ($T_i$) or flexibility can be evaluated by the ratio of the total grid sizes to the total noncovalent interactions along the same polypeptide chain.

The results demonstrate that Trikafta could rescue both gating and thermal defects of ΔF508 by coupling tightened cytoplasmic TMD1-TMD2 interactions to tightened Mg/ATP-mediated NBD1-NBD2 dimerization via the specific binding of the dynamic phosphorylated S813 site of

the R domain to the ICL1-ICL4 interface, which is a target of curcumin (38). This coupling pathway, combined with other therapeutic strategies such as curcumin, not only improves CFTR thermal stability but also shows promise for long-term therapeutic benefits in managing cystic fibrosis. Thus, thermodynamic modeling can be utilized to understand drug action mechanisms and update protein correction strategies.

## RESULTS

### NBD1-ICL4 interactions fail to increase the melting threshold of hNBD1

The isolated hNBD1-Δ(RE, RI) (PDB, 2PZE) is a single polypeptide spanning from S386 to G646 with a segment deleted from 405 to 436 (28). In contrast, the dephosphorylated hNBD1 in full-length CFTR (PDB, 5UAK) has disordered RI (403-438) (14). Therefore, in the absence of Mg/ATP-mediated NBD1-NBD2 dimerization, it is interesting to compare their melting temperature thresholds and evaluate the effect of NBD1-ICL4 interactions alone on the thermal stability of hNBD1.

In the dephosphorylated state, NBD1 is separated from NBD2 by the R domain (14). Without Mg/ATP bound, NBD1 had 17 intra-domain non-covalent interactions via amino acid side chains such as seven H-bonds, two salt bridges and eight π interactions (Figures 1a & Table S1). Most of these noncovalent interactions formed smaller thermorings. Notably, a smaller $Grid_5$ had a 5-residue size to control the F508-R560 and Y517-Y563 π bridges via a thermoring from F508 to Y512, Y517, Y563, R560 and back to F508. In contrast, some H-bonds generated bigger thermorings. For example, when the side chain of S495 H-bonded with the side chain of R553, a bigger $Grid_{18}$ had an 18-residue size to control the S495-R553 H-bond via a thermoring from S495 to F508, R560, R553, and back to S495. Thus, despite a total of 17 noncovalent interactions along the polypeptide chain from S384 to M645, a total of 81 grid sizes still resulted in an unusually high systematic thermal instability ($T_i$) of 4.76 (Table 1). That may be the reason why the crystal X-ray structure of isolated hNBD1-Δ(RE, RI) is unavailable in the absence of Mg/ATP (28).

In addition to the intra-domain noncovalent interactions, there were also noncovalent interactions between NBD1 and ICL4 (Figure 1b). These interactions included a salt bridge between E474 and R1066, an H-bond between E504 and Y1073, and seven π interactions such as M469-W1063, L1065-F1074-Y1073, F1068-F508-Y1073/F1074 and R1070-F508. Notably, F508, Y1073 and F1074 created the smallest triangle thermoring to stabilize the NBD1-ICL4

interface. In this case, it is necessary to examine whether these interfacial interactions affect the melting temperature threshold ($T_{m,th}$) of NBD1.

When D443 in the N-terminal region H-bonded with Y627 in the C-terminal region of NBD1, the biggest $Grid_{21}$ structure was created (Figure 1c). This structure had a 21-residue size to be responsible for stabilizing the least-stable D443-Y627 and R450-D567 H-bonds via a thermoring from D443 to R450, D567, F575, F587, H609, E608, K612, H620, Y625, Y627, and back to D443 (Figure 1c-d). These two H-bonds, when energetically equivalent to 2.0 basic H-bonds, had a calculated melting temperature threshold ($T_{m,th}$) of 32 °C, matching the melting threshold of isolated hNBD1-Δ(RE, RI) as measured by DSC (Table 1) (9). Therefore, the presence of stronger NBD1-ICL4 interactions may not increase the melting temperature threshold of NBD1 in the absence of bound Mg/ATP.

**Dimerization of NBD1-NBD2 increases the melting threshold of NBD1 more than NBD1-NBD1 dimerization**

When hCFTR is phosphorylated for Mg/ATP-dependent NBD1-NBD2 dimerization, the NBD1 (PDB, 6MSM) from E384 to Q637 exhibits a disordered segment from 638 to 646 with the unstructured RI shifting from 403-438 to 410-434 (16). Despite this minor alteration in the primary sequence structure, the tertiary noncovalent structure of NBD1 remains comparable to that of the isolated hNBD1-Δ(RE, RI) when bound by Mg/ATP for NBD dimerization (Figures 2a & Table S2) (37).

Firstly, the Mg/ATP binding site remained intact. For instance, T465, Q493 and D572 formed a stable triangle via $Mg^{2+}$. Meanwhile, ATP connected W401, K464 and S466. Additionally, W401 engaged in a π interaction with L475. However, the T388-T390, S459-H620 and R487-D567 H-bonds, as well as the F446-Y627 and H484-L568 π interactions were disrupted. Instead, the E391-K447 H-bond and the M394-F446 and F400-F409 π interactions were observed.

Secondly, there were some common noncovalent bridges present near F508. These included the W496-F508 and Y512-Y517 π interactions, as well as the Y512-E514, Y517-E537 and D529-Q552/R555 H-bonds. However, the W496-R560 and I507-Y563 π interactions, as well as the N505-R560 and R518-E527 H-bonds were replaced with the F508-R560, Y517-I521, and F533-I539 π interactions along with the S557-R560 H-bond. In addition, the H-bond between K503 and Y512 was found to be a π bridge.

Thirdly, common noncovalent interactions were also observed near the $Mg^{2+}$ site. For example, Y569-M595, P574-F575-F587 and H609-F587/F575 π interactions, along with the E583-H609-T604 H-bonds. The only difference was that the D565-K598 salt bridge was substituted by the Q525-E585 H-bond.

Fourthly, in the C-terminal region of NBD1 only the F626-L633 π interaction and the T629-S631 H-bond were intact. The H620-F640-Y625 π interactions were absent, as well as the D639-S641/S642 H-bonds, but the Y625-Q637 H-bond appeared.

Most importantly, although most of the NBD1-ICL4 interactions were maintained upon R domain phosphorylation with the exception of the replacement of the E504-Y1073 H-bond with the L1065-F1074 π interaction (Figure 2b), the biggest $Grid_{13}$ in the isolated hNBD1 was dissociated along with the broken F446-Y627 and S459-H620 bridges at the interface between the C- and N- termini. Instead, the biggest $Grid_8$ was present along with the least-stable F400-F409 π interaction (Figure 2a). It had an 8-residue size to control the π bridge via a thermoring from F400 to F409 and back to F400 (Figures 2c-d). With 1.2 equivalent basic H-bonds sealing it, the calculated melting temperature threshold ($T_{m,th}$) was about 50 °C, higher than the melting threshold of 48 °C measured by DSC for the isolated hNBD1-Δ(RE, RI) homodimer (Table 1) (9, 28). Meanwhile, the systematic thermal instability ($T_i$) of NBD1 dramatically decreased from 4.76 to 2.03 along with a total of 36 non-covalent bridges and 73 grid sizes (Table 1). Therefore, NBD1, when dimerized with NBD2, had a higher $T_{m,th}$ compared to when it dimerizes with itself.

**Dimerization of NBD1-NBD2 also increases the melting threshold of NBD1 lacking F508 more than NBD1-NBD1 dimerization does**

When F508 was deleted to disrupt the W496-F508-R560 π interactions, in the presence of Trikafta, the biggest $Grid_8$ was dissociated allosterically. This also led to the disruption of the Q525-E585 H-bond and the shift of the S557-R560 H-bond to the N505-R560 one (Figures 3a & Table S3). As a result, the H-bond moved from E391-K447 to N396-D443 near the same Mg/ATP site along with a new salt bridge between R487 and D567, a new H-bond between E449 and Q452, and a new π interaction between F446 and L454.

When this conformational change transmitted to the C-terminal region of NBD1, the T604-H609, Y625-Q637 and T629-S631 H-bonds along with the F626-L633 π interaction were disconnected. Meanwhile, a new T629-E632 H-bond and new K611-F630 and H620-Y625 π

interactions were produced. Overall, although the total number of noncovalent interactions decreased from 36 to 33 along the polypeptide chain from E391 to Q637, the total grid sizes increased from 73 to 81 (Figure 3a). Thus, the systematic thermal instability ($T_i$) or flexibility of NBD1 still increased from 2.03 to 2.45 despite the presence of Trikafta (Table 1).

On the other hand, the removal of F508 also disrupted most of the NBD1-ICL4 interactions except for the M469-W1063 π interaction. Additionally, the E474-R1066 H-bond was replaced with the Y380-R1066 π interaction (Figure 3b). Despite these weakened interfacial interactions between NBD1 and ICL4, the biggest $Grid_{15}$ was present in the N-terminal region. With a 15-residue size controlling the least-stable N396-D443 H-bond which was equivalent to 2.0 basic H-bonds, the calculated melting threshold for the thermoring from N396 to W401, S466, ATP, K464, L454, F446, D443, and back to N396 was about 44 °C, which was higher than the melting threshold of 40 °C of the isolated (F508del)hBVD1-Δ(RE, RI) homodimer measured by DSC (Table 1) (9). Hence, the NBD1-NBD2 dimerization in the presence of Trikafta also increased the melting threshold of NBD1 without F508 by 4 °C compared to NBD1-NBD1. The next question is how Trikafta achieves this when binding to TMD1 and TMD2, rather than NBD1, the NBD1-NBD2 interface or the NBD1-ICL4 interface.

**Tight NBD1-NBD2 dimerization primes the higher melting threshold of NBD1**

A previous study demonstrated that two isolated NBD1 polypeptides can form a head-to-tail homodimer in the presence of Mg/ATP when the RE and RI regions are deleted (28). However, the noncovalent interactions between two NBD1 polypeptides are limited to the Mg/ATP site. On one side of the interface, the Walker A half-site shows extensive interactions along the phosphates, $Mg^{2+}$ and the Walker A residues such as K464, T465 and S466. On the other side, the signature LSGGQ half-site also interacts with the phosphates through H-bonds (28).

However, when NBD1 and NBD2 dimerized, more noncovalent interactions were found between them regardless of the presence of F508del and Trikafta. In addition to the traditional interactions between the phosphates and the Walker A/B half-site or the signature LSHGH/ LSGGQ half-site (39), some new noncovalent interactions were also observed nearby (Figure 4). For example, the D529-R1245 and R555-T1246 H-bonds near the Walker A half-site and the T460-T1380 H-bond near the Walker B half-site. More importantly, Y577 from NBD1 formed a strong π–π interaction with H1375 from NBD2. The same Y577-H1375 π–π interaction was also found in ΔF508-hCFTR/E1371Q with Mg/ATP/VX-445/VX-809 bound or hCFTR/E1371Q with

Mg/ATP bound. However, the R555-T1246 and T460-T1380 H-bonds and the Y577-H1375 π interaction, together with the traditional interactions between the phosphates and the signature LSHGH half-site, were disrupted in ΔF508-hCFTR/E1371Q with Mg/ATP/VX-445 bound (Figure 4), and the Y577-Y577' π interaction is not shown in the isolated hCFTR-Δ(RE,RI) homodimers with or without F508 (28). In that regard, it is reasonable that NBD1 was stabilized along with increased melting temperature thresholds, 50 °C for hCFTR/E1371Q and 44 °C for ΔF508-hCFTR/E1371Q (Table 1). Given that the same Y577-H1375 π–π interaction was also absent in the partially dimerized NBD1 and NBD2 of ΔF508-hCFTR/E1371Q with Mg/ATP/VX-445 bound (Figure 4), it may serve as a critical clue to the correction pathway of ΔF508-CFTR by Trikafta.

**Specific fit of the dynamic phosphorylated S813 site to the TMD1/TMD2/NBD1 interfaces prime tight NBD1-NBD2 dimerization**

A recent cryo-EM structure revealed that when the PKA catalytic subunit (PKA-C) stabilizes the open state of phosphorylated hCFTR, the phosphate group of S813 is positioned between R487/K564 of NBD1 and R1070 of TMD2 at the NBD1/ICL4 interface (40). However, when the phosphorylated S813 site was introduced into the structure 8EIQ, the phosphate group of S813 was unable to form a salt bridge with R487 and K564 of NBD1 or R1070 of TMD2 in the phosphorylated ΔF508 hCFTR/E1371Q with Mg/ATP/Trikafta bound, which is necessary for tight NBD1-NBD2 dimerization. Instead, it was located between K162 and K166 at ICL1 while Y808 was involved in potential strong π interactions with R1066 at ICL4 and Y380 at the TMD1-NBD1 linker or the distal N-terminal tail of NBD1. Furthermore, R811 H-bonded with E54 and D58 at the N-terminal tail of TMD1. Thus, the phosphorylated S813 site bridged the ICL1/ICL4 interface with the N-terminal tails of TMD1 and NBD1. This bridge was also observed in hCFTR/E1371Q with Mg/ATP bound and ΔF508-hCFTR/E1371Q with Mg/ATP/VX-445/VX-809 bound but not in ΔF508-hCFTR/E1371Q with Mg/ATP/VX-445 bound (Figure 5). This induced fit of the dynamic phosphorylated S813 site to the TMD1/TMD2/NBD1 interfaces of hCFTR/E1371Q may explain why the E54A or D58A or E54A/D58A mutation inhibits the binding of the R domain to the N-terminal tail and the related hCFTR activity (41), and why mutations such as K166A/H, R1066H, S813D/Y808A and S813D/R811A suppress curcumin potentiation of hCFTR activity when curcumin is bound to this S813 binding site (38).

**Strong cytoplasmic TMD1-TMD2 interactions promote the specific fit of the dynamic phosphorylated S813 site to the TMD1/TMD2/NBD1 interfaces favoring maximal channel activity**

Our previous study showed that K190 and K978 are located in the tetrahelix bundle of hCFTR. Constitutive gain of function (GOF) mutations such as K978C and K190C significantly stimulate ATP-independent but PKA-dependent channel activation, thereby increasing ATP and PKA sensitivity allosterically. Importantly, these constitutive ICL mutations can restore the function of CFTR mutants like G551D without ATP binding and NBD2-free Δ1198 without NBD dimerization (42). They also prevent the irreversible thermal inactivation of ΔF508 hCFTR (10). All of this suggests that the tetrahelix bundle acts as a gating linchpin for ATP-independent but phosphorylation-dependent CFTR activation.

Since the extracellular gate remains closed in a cryo-EM structure of zebrafish CFTR (zCFTR) even after R domain phosphorylation and ATP binding allowing tight NBD1-NBD2 dimerization (39), this structure can serve as an ideal negative control to investigate how the tetrahelix bundle gates the CFTR channel in an ATP-independent but phosphorylation-dependent manner.

In the dephosphorylated closed state of wild type (WT) hCFTR, the segment 970-985 in TM9 was structured as an α-helix and connected with TM4 via the R251-D985 H-bond. R251 and S256 in TM4 were located on two separate α-helices. Similarly, T1053 and E1046 in TM10 were also positioned on two separate α-helices. The C-terminal region of the R domain was wedged among TMs 3, 4, 9, and 10 (Figure 6). This is reminiscent of the inhibitory lipid at the active vanilloid site in heat-gated transient receptor potential vanilloid-1 (TRPV1) or 3 (TRPV3) bio-thermometers (33-34).

When phosphorylation released the R domain for channel opening, both TM4 and TM10 underwent a π-to-α transition. In addition to the R251-D985 H-bond, R1048 also formed H-bonds with both N974 and D979 via their side chains, leading to a smaller $Grid_4$. Meanwhile, N189 H-bonded with E1044, F976 formed a CH-π interaction with T262, and Q179 H-bonded with S256 via their side chains. However, T1053 H-bonded with the backbone NH at G970. Notably, K1060 linked with E267 via an H-bond, confirming the previous report (Figure 6) (43).

In contrast, when exposed to Mg/ATP agonists that stimulate the phosphorylated zCFTR, the loose α-helix in TM9 extended to D987 (D979 in hCFTR), and segments 1052-1056 and 1057-

K1068 in TM10 formed two α-helices. In this case, most noncovalent interactions were disrupted, including the D987-R1056-N982 (D979-R1048-N974 in hCFTR) H-bonds and the F984-T263 (F976-T262 in hCFTR) π interaction. Instead, only the E1052-R1056, R979-E1054 and G978-S1061 H-bonds were present in this pre-open closed state despite the well-known R554-T1247 (R555-T1246 in hCFTR) H-bond (39) (Figures 4 and S1). Therefore, the tight cytoplasmic TMD1-TMD2 interactions were required for CFTR opening.

Since there is no gap between TMD1 and TMD2 of phosphorylated ΔF508-hCFTR upon Trikafta and Mg/ATP binding (22), it is necessary to examine if Trikafta tightens the cytoplasmic TMD1-TMD2 interactions. The study on the tertiary structure of this activated mutant indicated that despite the disruption of the F976-T262 π interaction and the Q179-S256 and E267-K1060 H-bonds, TM10 exhibited two α–helices at the T1053-E1046 interface. This allowed for new R975-E1046 and E1044-N186 H-bonds at the TM9-TM10-TM3 interface. Thus, a much smaller $Grid_1$ produced a more thermally stable triangle among N974, R975, E1046, and R1048 (Figure 6). Since VX-809 alone stimulates ΔF508-CFTR activity in the absence of tight NBD dimerization (22, 26), the gating defect of ΔF508-hCFTR was first rescued upon the tight cytoplasmic TMD1-TMD2 interactions before the thermal defect of NBD1 was corrected.

Further detailed studies showed that all three modulators in Trikafta worked together to enhance this unique cytoplasmic H-bond network through their specific noncovalent interactions with TMD1 and TMD2 (Figure S2), which were similar to previous reports (22, 44-46). The same H-bond network was also observed in ΔF508-hCFTR/E1371Q with Mg/ATP/VX-445/VX-809 bound for tight NBD dimerization. However, it was compromised in ΔF508-hCFTR/E1371Q with Mg/ATP/VX-445 bound for partial NBD1-NBD2 dimerization (Figure 4). Thus, once Trikafta binding tightened the cytoplasmic TMD1-TMD2 interactions, the dynamic phosphorylated S813 site could fit into the ICL1/ICL4/NBD1 interfaces for the tight NBD1-NBD2 interactions.

## DISCUSSION

F508 in NBD1, like F251 in β-D-glucoside glucohydrolase (46), plays a central role in CFTR expression on the cell surface and ATP/PKA-mediated channel activity. The deletion of F508 (ΔF508) on the surface of NBD1 destabilizes NBD1 and the nearby interdomain interactions, leading to both thermal and gating defects (17-21). Thus, rescuing strategies have focused on this

domain and its interfaces (20, 47-51). Although Trikafta modulators do not target them, they successfully correct both defects of phosphorylated ΔF508-CFTR even at 37 °C along a significantly different pathway (23-27). This study demonstrated that Trikafta binding to flexible TMD1 and TMD2 stabilized the most flexible NBD1 by reinforcing specific phosphorylation-dependent interdomain interactions, rescuing defects of F508del with improved channel opening and chloride ion transport. These gating features are vital for maintaining airway surface liquid homeostasis and overall lung function. Although the deletion of F508 causes the primary thermal defect in NBD1 and then the gating defect at the TMD1/TMD2 interface, Trikafta rescued them in a reverse manner allosterically.

**Specific binding of the dynamic phosphorylated S813 site to the TMD1/TMD2/NBD1 interfaces is necessary for the normal gating pathway**

Mg/ATP-mediated NBD1-NBD2 dimerization is required for the normal channel opening of phosphorylated CFTR (14-16). However, recent simultaneous kinetic studies of NBD isomerization and channel gating have shown that CFTR quickly transitions to a flicker-closed state upon NBD dimerization (52). Consistent with this finding, zCFTR remains closed even when NBD1 and NBD2 are tightly dimerized by Mg/ATP binding at their interface (39).

On the other hand, our previous studies have highlighted the significance of constitutive mutations K190C and K978C at the TMD1/TMD2 interface in ATP-independent but phosphorylation-dependent hCFTR activation (42), as well as the significance of the E267-K1060 salt-bridge at this interface in allosterically coupling to R domain phosphorylation (43). This study further suggests that tight cytoplasmic TMD1-TMD2 interactions are crucial for CFTR opening and are linked to specific interactions of the dynamic phosphorylated S813 site with ICL1, ICL4 and the distal N-terminal tails of TMD1 and NBD1 (Figures 5-7).

Moreover, the phosphorylated R domain has been found near the ICL1-ICL4 interface of not only the open E1371Q-hCFTR but also the glutathione transporter Yeast Cadmium Factor 1 (Ycf1) E1435Q mutant (16, 53), Therefore, the flexible cytoplasmic TMD1-TMD2 interface cannot guarantee strict coupling between NBD dimerization and channel opening. Specific binding of the dynamic phosphorylated S813 site to the TMD1/TMD2/NBD1 interfaces is necessary to enhance cytoplasmic TMD1-TMD2 interactions for normal channel opening (Figure 7).

**Specific binding of the dynamic phosphorylated S813 site to the TMD1/TMD2/NBD1 interfaces is also necessary for the Trikafta correction pathway**

This study further indicated that despite the weakened NBD1-ICL4 interactions in ΔF508 CFTR, the tight cytoplasmic TMD1-TMD2 interactions in ΔF508 CFTR/E1371Q were not restored by VX-445 until the combination of VX-445 and VX-809 or Trikafta (VX-445, VX-661 and VX-770) were bound to TMD1 and TMD2 (Figure 6). Along with these interactions, the specific interactions of the dynamic phosphorylated S813 site with ICL1, ICL4 and the distal N-terminal tails of TMD1 and NBD1 and Mg/ATP-mediated tight NBD1-NBD2 dimerization were also observed in ΔF508 CFTR/E1371Q with VX-445 and VX-809 or Trikafta bound rather than VX-445 alone bound (Figures 4-5). Therefore, similar to lysine ligation to the heme iron in cytochrome c (54), remote Trikafta binding to flexible regions of TMD1 and TMD2 may reinforce the cytoplasmic TMD1-TMD2 interactions, favoring the specific binding of the dynamic phosphorylated S813 site to the TMD1/TMD2/NBD1 interfaces and NBD dimerization that further stop irreversible thermal inactivation by stabilizing NBD1 (Figure 7) (10, 12, 37). Based on this important role of the cytoplasmic TMD1/TMD2 interactions, it is reasonable to find some CF-causing mutations G970E/D, D979V, E1044X, E1046X, and T1053I are involved (http://www.genet.sickkids.on.ca/cftr; https://cftr2.org).

**Role of a curcumin-like drug in optimizing cystic fibrosis treatment**

Curcumin can strengthen the stimulatory interactions between the dynamic phosphorylated S813 site and the ICL1/ICL4 interface to stabilize the open state (38, 55). However, curcumin can also stabilize the stochastic, competitive and stimulatory binding of the phosphorylated S795 site to these interfaces (38). This may explain why curcumin alone is not effective in maintaining ΔF508 CFTR activity at room temperature (56), or preventing the irreversible thermal inactivation of ΔF508-hCFTR at physiological temperature (10).

On the other hand, Trikafta modulators maintain higher ΔF508-hCFTR activity even at a physiological temperature of 37 °C (23-27). Therefore, specific interactions of the dynamic phosphorylated S813 site with not only the ICL1-ICL4 interface but also the distal N-terminal tails of TMD1 and NBD1 may be necessary to couple tight cytoplasmic TMD1-TMD2 interactions to Mg/ATP-mediated NBD1-NBD2dimerization at human body temperature. In support of this proposal, when a strong water-like spherical density at the NBD1/TMD1/TMD2 interfaces was observed at a low temperature of 4 °C (22), more protein-water H-bonds were also reported in the cold-denatured state of yeast frataxin than in the hot-denatured state (57). Thus, although a low temperature may hydrate the NBD1/TMD1/TMD2 interfaces through an interfacial H-bonding

network between the ordered water molecules and the charged residues such as K162, K166, E54, D58 or R0166, a high temperature may dehydrate these interfaces, allowing specific binding of the dynamic phosphorylated S813 site to the NBD1/TMD1/TMD2 interfaces to be captured in a cryo-EM structure at a physiological temperature. Most importantly, once this specific binding can be stabilized by a drug like curcumin, a combined therapy of Trikafta with this drug may further optimize cystic fibrosis treatment through improved protein durability and drug efficacy. Further molecular dynamics (MD) simulations are necessary to accurately understand the role of the dynamic binding of the phosphorylated S813 site to the NBD1/TMD1/TMD2 interfaces in the normal gating pathway of native CFTR and the correction pathway of ΔF508-CFTR by Trikafta.

## CONCLUSIONS

The ability of combination therapy to correct the thermal and gating defects of misfolded CFTR is essential for the optimal treatment of cystic fibrosis. While Trikafta modulators have been approved to treat the most common cystic fibrosis mutation F508del-CFTR, less is known about the exact rescuing pathway. This study demonstrated that Trikafta binding can correct functional defects by enhancing specific phosphorylation-dependent interdomain interactions to stabilize the most flexible domain in the mutant allosterically. These findings highlight the importance of post-translational chemical modifications in protein function. Targeting this correction pathway could be a promising approach for developing new therapies for patients with CF who have similar or different CFTR mutations.

## COMPUTATIONAL METHODS

### Data mining resources

Three cryo-EM structures of human CFTR (hCFTR) constructs with or without F508 at 4 °C were chosen for thermoring analysis. These structures included dephosphorylated hCFTR in a closed state (PDB ID, 5UAK, model resolution = 3.87 Å) (14), phosphorylated E1371Q with Mg/ATP bound in an open state (PDB ID, 6MSM, model resolution = 3.2 Å) (16), and phosphorylated hCFTR/E1371Q/ΔF508 with Mg/ATP/Trikafta bound in an open state (PDB ID, 8EIQ, model resolution = 3.0 Å) (22). Additionaly, the cryo-EM structure of zebrafish CFTR (zCFTR) construct with phosphorylation and Mg/ATP bound (PDB, 5W81, model resolutions 3.4 Å) was used as a control to indicate the role of the cyroplasmic TMD1/TMD2 interface (39). Finally, the

cryo-EM structure of phosphorylated hCFTR with Mg/ATP/PKA-C bound (PDB, 9DW9, model resolution = 2.8 Å) was also used to fit the dynamic phosphorylated S813 site to the NBD1/TMD1/TMD2 interfaces (40).

**Standard methods for filtering non-covalent interactions**

The standard methods for filtering non-covalent interactions, along with exact calculations, were the same as those previously used, ensuring accurate and repeatable results (30-37). UCSF Chimera was used to review potential stereo-selective or regio-selective intra-domain lateral noncovalent interactions along the single polypeptide chain of hNBD1 with or without F508. These interactions included salt bridges, H-bonds and lone pair/CH/cation-π interactions between paired amino acid side chains. When a backbone NH at a residue position was within a cutoff distance for an H-bond with a side chain of a nearby residue, that H-bond was also considered. Detailed cutoff distances and interaction angles can be obtained in the online Supporting Information (Tables S1, S2, and S3). In this study, approximately at least 16 different noncovalent interactions were identified along the single polypeptide chain from L383 to L644 of NBD1 on each protomer.

**Mapping the thermoring structures of NBD1 using the grid thermodynamic model**

The same grid thermodynamic model that was previously validated was used to map the thermoring structures of NBD1 in full-length CFTR (30-37). Briefly, filtered noncovalent interactions were placed in an adjacency matrix to create a systematic fluidic grid-like mesh network along the single polypeptide chain (black line) of NBD1 from L383 to L644. In this network, each node represented paired protein residues (colorful arrows) that formed a specific noncovalent interaction via their side chains, and each colorful edge represented a specific noncovalent interaction that formed a direct path. However, a reverse path represented a sequence of alternating polypeptide chain and links with no repeating nodes. In these representations, any link between two nodes had two path lengths that indicated the cost of traveling across the link. In this study, the path length was defined as the total number of free or silent amino acids that did not involve any noncovalent interactions between two nodes. Thus, the traveling cost across any link was determined by the reverse path length because the direct path length was zero, and any noncovalent inteaction with the alternating polypeptide chain lining a reverse path had a positively curved edge (58). For example, when F508 formed a π interaction with R560 in Figure 1a, if a

direct path started from F508 and ended at R560, the peptide segment from R560 to F508 paved a reverse path.

When multiple reverse paths exist for a specific noncovalent interaction, identifying the shortest reverse path is essential to minimize travel costs. This is achieved by Floyd-Warshall's Algorithm, which compares all possible adjacent reverse paths through the graph between each pair of nodes (59). In the case of the F508-R560 π interaction shown in Figure 1a, one adjacent reverse path from R560 to R553, S495, and F508 had a length of 18 (the total number of free amino acids in peptide segments 507 to 494 and 552 to 559). However, another adjacent reverse path from R560 to Y563, Y517, Y512, and F508 included Y512-Y517-Y563 π interactions, resulting in a length of 5 (the sum of free amino acids in peptide segments 509 to 511 and 562 to 561). Since no other possible adjacent reverse paths were shorter than 5, the shortest reverse path length for the F508-R560 bridge was determined to be 5.

Once the shortest reverse path was identified for each noncovalent interaction, the direct path and the shortest reverse path emerged as a thermosensitive ring or "thermoring" to control the heat unfolding of that noncovalent interaction. Since the shortest reverse path length was defined as the size of a thermoring, the thermoring was denoted as $Grid_s$. In this way, all noncovalent interactions could be tracked by their respective unshared thermoring sizes so that the biggest thermoring could be identified. As the least-stable noncovalent interaction in the biggest thermoring was typically the weakest link along the single polypeptide chain, a melting temperature threshold ($T_{m,th}$) of NBD1 could be calculated theoretically. Furthermore, when the total non-covalent interactions and grid sizes along the given polypeptide chain were displayed by black and cyan circles beside the mesh network map, the grid-based systematic thermal instability ($T_i$) could also be computed to evaluate the flexibility of NBD1.

**Calculation of the melting temperature threshold ($T_{m,th}$)**

The same empirical equation and coefficients used in previous studies on temperature-dependent structures were applied to calculate the melting temperature thresholds ($T_{m,th}$) for thermal unfolding of a specific grid (30-37):

$$T_{m,th}\ (°C) = 34 + (n - 2) \times 10 + (20 - s) \times 2 \quad (1)$$

where, n represents the total number of basic H-bonds (each approximately 1 kcal/mol) that are calculated to be approximately equal in stability of the least-stable noncovalent interaction

controlled by the given grid (60); and s is the grid size used to control the least-stable noncovalent interaction in the given grid.

**Evaluation of the grid-based systemic thermal instability ($T_i$)**

The same empirical equation used in previous studies on temperature-dependent structures was utilized to calculate the systematic thermal instability ($T_i$) along the given polypeptide chain (30-37):

$$T_i = S/N \quad (2)$$

where, S and N are the total grid sizes and the total non-covalent interactions along a specific polypeptide chain. This calculation allows for evaluation of the protein's compact conformational entropy or flexibility.

## ABBREVIATIONS

ABC, ATP-binding cassette

CF, cystic fibrosis

cryo-EM, cryoelectron microscopy

CFTR, cystic fibrosis transmembrane conductance regulator

DSC, differential scanning calorimetry

DSF, differential scanning fluorimetry

GOF, gain of function

hCFTR, human CFTR

ICL1, intracellular loop 1

ICL4, intracellular loop 4

MD, molecular dynamics

NBD1, nucleotide binding domain 1

NBD2, nucleotide binding domain 2

PKA, protein kinase A

PKA-C, the PKA catalytic subunit

R, regulatory

RE, regulatory extension

RI, regulatory insert

$T_i$, systematic thermal instability

$T_{m,th}$, melting temperature threshold

TMH, transmembrane helix

TMD1, transmembrane domain 1

TMD2, transmembrane domain 2

TRPV1, transient receptor potential vanilloid-1

TRPV3, transient receptor potential vanilloid-3

2-APB, 2-aminoethoxydiphenyl borate

WT, wild type

wtCFTR, wild type CFTR

Ycf1, Yeast Cadmium Factor 1

zCFTR, zebrafish CFTR

## REFERENCES


1. Riordan JR, Rommens JM, Kerem B, Alon N, Rozmahel R, Grzelczak Z, Zielenski J, Lok S, Plavsic N, Chou JL, et al. Identification of the cystic fibrosis gene: cloning and characterization of complementary DNA. *Science*. **245,** 1066-1073 (1989).
2. Anderson MP, Berger HA, Rich DP, Gregory RJ, Smith AE, Welsh MJ. Nucleoside triphosphates are required to open the CFTR chloride channel. *Cell*. **67**, 775-84. (1991).
3. Anderson MP, Gregory RJ, Thompson S, Souza DW, Paul S, Mulligan RC, Smith AE, Welsh MJ. Demonstration that CFTR is a chloride channel by alteration of its anion selectivity. *Science*. **253**, 202-5 (1991).
4. Meng X, Clews J, Kargas V, Wang X, Ford RC. The cystic fibrosis transmembrane conductance regulator (CFTR) and its stability. *Cell Mol Life Sci.* **74**, 23-38 (2017).
5. Kerem B, Rommens JM, Buchanan JA, Markiewicz D, Cox TK, Chakravarti A, Buchwald M, Tsui LC. Identification of the cystic fibrosis gene: genetic analysis. *Science.* **245**, 1073-80 (1989).
6. Dalemans W, Barbry P, Champigny G, Jallat S, Dott K, Dreyer D, Crystal RG, Pavirani A, Lecocq JP, Lazdunski M. Altered chloride ion channel kinetics associated with the delta F508 cystic fibrosis mutation. *Nature* **354,** 526–528 (1991).
7. Lukacs GL, Chang XB, Bear C, Kartner N, Mohamed A, Riordan JR, Grinstein S. The delta F508 mutation decreases the stability of cystic fibrosis transmembrane conductance regulator in the plasma membrane. Determination of functional half-lives on transfected cells. *J Biol Chem*. **268**, 21592-8 (1993).
8. Sharma M, Benharouga M, Hu W, Lukacs GL. Conformational and temperature-sensitive stability defects of the delta F508 cystic fibrosis transmembrane conductance regulator in post-endoplasmic reticulum compartments. *J Biol Chem.* **276**, 8942-50 (2001).
9. Protasevich I, Yang Z, Wang C, Atwell S, Zhao X, Emtage S, Wetmore D, Hunt JF, Brouillette CG. Thermal unfolding studies show the disease causing F508del mutation in CFTR thermodynamically destabilizes nucleotide-binding domain 1. *Protein Sci.* **19,** 1917-1931 (2010).
10. Wang W, Okeyo GO, Tao B, Hong JS, Kirk KL. Thermally unstable gating of the most common cystic fibrosis mutant channel (ΔF508): "rescue" by suppressor mutations in

nucleotide binding domain 1 and by constitutive mutations in the cytosolic loops. *J Biol Chem.* **286**, 41937-41948 (2011).

11. Rabeh WM, Bossard F, Xu H, Okiyoneda T, Bagdany M, Mulvihill CM, Du K, di Bernardo S, Liu Y, Konermann L, Roldan A, Lukacs GL. Correction of both NBD1 energetics and domain interface is required to restore ΔF508 CFTR folding and function. *Cell*. **148**,150-163 (2012).
12. Liu X, Dawson DC. Cystic fibrosis transmembrane conductance regulator (CFTR) potentiators protect G551D but not ΔF508 CFTR from thermal instability. *Biochemistry*. **53**, 5613-8 (2014).
13. Froux L, Coraux C, Sage E, Becq F. Short-term consequences of F508del-CFTR thermal instability on CFTR-dependent transepithelial currents in human airway epithelial cells. *Sci Rep.* **9**, 13729 (2019).
14. Liu F, Zhang Z, Csanády L, Gadsby DC, Chen J. Molecular Structure of the Human CFTR Ion Channel. *Cell*. **169,** 85-95.e8 (2017).
15. Vergani P, Lockless SW, Nairn AC, Gadsby DC. CFTR channel opening by ATP-driven tight dimerization of its nucleotide-binding domains. *Nature* **433**, 876-80 (2005).
16. Zhang Z, Liu F, Chen J. Molecular structure of the ATP-bound, phosphorylated human CFTR. *Proc Natl Acad Sci U S A.* **115,** 12757-12762 (2018).
17. Du K, Sharma M, Lukacs GL. The DeltaF508 cystic fibrosis mutation impairs domain-domain interactions and arrests post-translational folding of CFTR. *Nat Struct Mol Biol.* **12**, 17-25 (2005).
18. Cui L, Aleksandrov L, Chang XB, Hou YX, He L, Hegedus T, Gentzsch M, Aleksandrov A, Balch WE, Riordan JR. Domain interdependence in the biosynthetic assembly of CFTR. *J Mol Biol.* **365**, 981–994 (2007).
19. Jih KY, Li M, Hwang TC, Bompadre SG. The most common cystic fibrosis-associated mutation destabilizes the dimeric state of the nucleotide-binding domains of CFTR. *J Physiol.* **589**(Pt 11), 2719-31 (2011).
20. He L, Aleksandrov AA, An J, Cui L, Yang Z, Brouillette CG, Riordan JR. Restoration of NBD1 thermal stability is necessary and sufficient to correct ΔF508 CFTR folding and assembly. *J Mol Biol.* **427**, 106-20. (2015)

21. Soya N, Xu H, Roldan A, Yang Z, Ye H, Jiang F, Premchandar A, Veit G, Cole SPC, Kappes J, Hegedüs T, Lukacs GL. Folding correctors can restore CFTR posttranslational folding landscape by allosteric domain-domain coupling. *Nat Commun.* **14**, 6868. (2023)
22. Fiedorczuk K, Chen J. Molecular structures reveal synergistic rescue of Δ508 CFTR by Trikafta modulators. *Science*. **378**, 284-290 (2022).
23. Keating D, Marigowda G, Burr L, Daines C, Mall MA, McKone EF, Ramsey BW, Rowe SM, Sass LA, Tullis E, McKee CM, Moskowitz SM, Robertson S, Savage J, Simard C, Van Goor F, Waltz D, Xuan F, Young T, Taylor-Cousar JL; VX16-445-001 Study Group. VX-445-Tezacaftor-Ivacaftor in Patients with Cystic Fibrosis and One or Two Phe508del Alleles. *N Engl J Med.* **379**, 1612-1620 (2018).
24. Middleton PG, Mall MA, Dřevínek P, Lands LC, McKone EF, Polineni D, Ramsey BW, Taylor-Cousar JL, Tullis E, Vermeulen F, Marigowda G, McKee CM, Moskowitz SM, Nair N, Savage J, Simard C, Tian S, Waltz D, Xuan F, Rowe SM, Jain R; VX17-445-102 Study Group. Elexacaftor-Tezacaftor-Ivacaftor for Cystic Fibrosis with a Single Phe508del Allele. *N Engl J Med.* **381**,1809-1819 (2019).
25. Bose SJ, Bijvelds MJC, Wang Y, Liu J, Cai Z, Bot AGM, de Jonge HR, Sheppard DN. Differential thermostability and response to cystic fibrosis transmembrane conductance regulator potentiators of human and mouse F508del-CFTR. *Am J Physiol Lung Cell Mol Physiol.* **317**, L71-L86 (2019).
26. Veit G, Roldan A, Hancock MA, Da Fonte DF, Xu H, Hussein M, Frenkiel S, Matouk E, Velkov T, Lukacs GL. Allosteric folding correction of F508del and rare CFTR mutants by elexacaftor-tezacaftor-ivacaftor (Trikafta) combination. *JCI Insight.* **5**, e139983. (2020).
27. Veit G, Vaccarin C, Lukacs GL. Elexacaftor co-potentiates the activity of F508del and gating mutants of CFTR. *J Cyst Fibros*. **20**, 895-898 (2021).
28. Atwell S, Brouillette CG, Conners K, Emtage S, Gheyi T, Guggino WB, Hendle J, Hunt JF, Lewis HA, Lu F, Protasevich II, Rodgers LA, Romero R, Wasserman SR, Weber PC, Wetmore D, Zhang FF, Zhao X. Structures of a minimal human CFTR first nucleotide-binding domain as a monomer, head-to-tail homodimer, and pathogenic mutant. *Protein Eng Des Sel.* **23,** 375-384 (2010).

29. Soya N, Roldan A, Lukacs GL. Differential Scanning Fluorimetry and Hydrogen Deuterium Exchange Mass Spectrometry to Monitor the Conformational Dynamics of NBD1 in Cystic Fibrosis. *Methods Mol Biol*. **1873**, 53-67 (2019).
30. Wang G The network basis for the structural thermostability and the functional thermoactivity of aldolase B. *Molecules.* **28,** 1850 (2023).
31. Wang G. Network basis for the heat-adapted structural thermostability of bacterial class II fructose bisphosphate aldolase. *ACS Omega.* **8,** 17731–17739 (2023).
32. Wang G. Thermal ring-based heat switches in hyperthermophilic class II bacterial fructose aldolase. *ACS Omega.* **8**, 24624–24634 (2023).
33. Wang G. Thermoring-Based Heat Activation Switches in the TRPV1 Biothermometer. *Int. J. Biol. Macromol.* **248,** 125915 (2023).
34. Wang G. Thermoring basis for the TRPV3 bio-thermometer. *Sci Rep.* **13,** 21594 (2023).
35. Wang G. Phosphatidylinositol-4,5-biphosphate ($PIP_2$)-Dependent Thermoring Basis for Cold-Sensing of the Transient Receptor Potential Melastatin-8 (TRPM8) Biothermometer. *Physchem.* **4,** 106–119 (2024).
36. Wang G. Thermoring basis for heat unfolding-induced inactivation in TRPV1. *Nat. Sci*.**4**, e20240008 (2024).
37. Wang G. ATP-dependent thermoring basis for the heat unfolding of the first nucleotide-binding domain isolated from CFTR. *Research Square.* https://doi.org/10.21203/rs.3.rs-5479740/v1 (2024).
38. Wang G. Molecular Basis for Fe(III)-Independent Curcumin Potentiation of Cystic Fibrosis Transmembrane Conductance Regulator Activity. *Biochemistry.* **54,** 2828-2840. Erratum in: *Biochemistry*. **54**, 4161 (2015).
39. Zhang Z, Liu F, Chen J. Conformational Changes of CFTR upon Phosphorylation and ATP Binding. *Cell.* **170(3),** 483-491.e8. (2017).
40. Fiedorczuk K, Iordanov I, Mihályi C, Szöll} osi A, Csanády L, Chen J. The structures of protein kinase A in complex with CFTR: Mechanisms of phosphorylation and reversible activation. *Proc Natl Acad Sci USA.* **121,** e2409049121 (2024).
41. Naren AP, Cormet-Boyaka E, Fu J, Villain M, Blalock JE, Quick MW, Kirk KL. CFTR chloride channel regulation by an interdomain interaction. *Science* **286**, 544-8 (1999).

42. Wang W, Wu J, Bernard K, Li G, Wang G, Bevensee MO, Kirk KL. ATP-independent CFTR channel gating and allosteric modulation by phosphorylation. *Proc Natl Acad Sci U S A.* **107**, 3888-3893 (2010).
43. Wang W, Roessler BC, Kirk KL. An electrostatic interaction at the tetrahelix bundle promotes phosphorylation-dependent cystic fibrosis transmembrane conductance regulator (CFTR) channel opening. *J Biol Chem.* **289**, 30364-30378 (2014).
44. Liu, F., Zhang, Z., Levit, A., Levring, J., Touhara, K.K., Shoichet, B.K., and Chen, J. Structural identification of a hotspot on CFTR for potentiation. *Science* **364**, 1184–1188 (2019).
45. Fiedorczuk K, Chen J. Molecular structures reveal synergistic rescue of Δ508 CFTR by Trikafta modulators. *Cell* **185**, 158–168 (2022).
46. Souza VP, Ikegami CM, Arantes GM, Marana SR. Protein thermal denaturation is modulated by central residues in the protein structure network. *FEBS J.* **283**, 1124-38 (2016).
47. Sampson HM, Robert R, Liao J, Matthes E, Carlile GW, Hanrahan JW, Thomas DY. Identification of a NBD1-binding pharmacological chaperone that corrects the trafficking defect of F508del-CFTR. *Chem Biol.* **18**, 231-42 (2011).
48. Hall JD, Wang H, Byrnes LJ, Shanker S, Wang K, Efremov IV, Chong PA, Forman-Kay JD, Aulabaugh AE. Binding screen for cystic fibrosis transmembrane conductance regulator correctors finds new chemical matter and yields insights into cystic fibrosis therapeutic strategy. *Protein Sci.* **25**, 360-373 (2016).
49. Ehrhardt A, Chung WJ, Pyle LC, Wang W, Nowotarski K, Mulvihill CM, Ramjeesingh M, Hong J, Velu SE, Lewis HA, Atwell S, Aller S, Bear CE, Lukacs GL, Kirk KL, Sorscher EJ. Channel Gating Regulation by the Cystic Fibrosis Transmembrane Conductance Regulator (CFTR) First Cytosolic Loop. *J Biol Chem.* **291**, 1854-1865 (2016).
50. Carlile GW, Yang Q, Matthes E, Liao J, Radinovic S, Miyamoto C, Robert R, Hanrahan JW, Thomas DY. A novel triple combination of pharmacological chaperones improves F508del-CFTR correction. *Sci Rep.* **8**, 11404 (2018).
51. Padányi R, Farkas B, Tordai H, Kiss B, Grubmüller H, Soya N, Lukács GL, Kellermayer M, Hegedűs T. Nanomechanics combined with HDX reveals allosteric drug binding sites of CFTR NBD1. *Comput Struct Biotechnol J.* **20**, 2587-2599 (2022).

52. Levring J, Terry DS, Kilic Z, Fitzgerald G, Blanchard SC, Chen J. CFTR function, pathology and pharmacology at single-molecule resolution. *Nature*. **616**, 606-614 (2023). Erratum in: *Nature*. **617**, E11 (2023).
53. Khandelwal NK, Millan CR, Zangari SI, Avila S, Williams D, Thaker TM, Tomasiak TM. The structural basis for regulation of the glutathione transporter Ycf1 by regulatory domain phosphorylation. *Nat Commun.* **13**, 1278 (2022).
54. Gu J, Shin DW, Pletneva EV. Remote Perturbations in Tertiary Contacts Trigger Ligation of Lysine to the Heme Iron in Cytochrome c. *Biochemistry* **56**, 2950-2966 (2017).
55. Wang G, Linsley R, Norimatsu Y. External $Zn^{2+}$ binding to cysteine-substituted cystic fibrosis transmembrane conductance regulator constructs regulates channel gating and curcumin potentiation. *FEBS J.* **283,** 2458-2475 (2016).
56. Wang W, Li G, Clancy JP, Kirk KL. Activating cystic fibrosis transmembrane conductance regulator channels with pore blocker analogs. *J Biol Chem.* **280**, 23622-30 (2005).
57. Camilloni C, Bonetti D, Morrone A, Giri R, Dobson CM, Brunori M, Gianni S, Vendruscolo M. Towards a structural biology of the hydrophobic effect in protein folding. *Sci Rep.* **6**, 28285 (2016).
58. Gosztolai A, Arnaudon A. Unfolding the multiscale structure of networks with dynamical Ollivier-Ricci curvature. *Nat Commun.*; **12,** 4561 (2021).
59. Floyd R. W. Algorithm-97 - Shortest path. *Commun Acm.* **5,** 345–345 (1962).
60. Neel AJ, Hilton MJ, Sigman MS, Toste FD. Exploiting non-covalent π interactions for catalyst design. *Nature.* **543**, 637-646 (2017).

## AUTHOR CONTRIBUTIONS

Guangyu Wang wrote the main manuscript text and prepared Figures. 1, 2, 3, 4, 5, 6, 7 and Table 1. Supporting Information (Tables S1, S2, S3; Figures S1, S2) and reviewed the manuscript.

## ACKNOWLEDGEMENTS

The author's own studies cited in this article were supported by the NIDDK Grant (DK45880 to D.C.D.) and the Cystic Fibrosis Foundation grant (DAWSON0210), the NIDDK grant (2R56DK056796-10) and the American Heart Association (AHA) Grant (10SDG4120011 to GW).

## CONFLICT OF INTEREST STATEMENT

The author declares no conflict of interest.

## ETHICS STATEMENT

The author confirms that he has followed the ethical policies of the journal.

## DATA AVAILABILITY STATEMENT

All data generated or analyzed during this study are included in this published article and Supporting Information.

ORCID Guangyu Wang https://orcid.org/0000-0002-5581-6926

## SUPPLEMENTARY INFORMATION

Additional supporting information can be found online in the Supporting Information section at the end of this article.

**Table 1** Grid thermodynamic model-based new parameters of NBD1 in hCFTR constructs.

| Construct | hCFTR | | |
|---|---|---|---|
| PDB ID | 5UAK | 6MSM | 8EIQ |
| F508 | + | + | - |
| E1371Q | - | + | + |
| Mg/ATP (10 mM)/PKA | - | + | + |
| Sampling temperature, °C | 4 | 4 | 4 |
| NBD dimerized | - | + | + |
| Normal $Mg^{2+}$ site | | + | - |
| Name of the biggest grid | $Grid_{21}$ | $Grid_{8}$ | $Grid_{15}$ |
| Grid size (s) | 21 | 8 | 15 |
| # of energetically equivalent basic H-bonds (n) controlled by $Grid_s$ | 2.0 | 1.2 | 2.0 |
| Total non-covalent interactions (N) | 17 | 36 | 33 |
| Total grid sizes (S), a.a. | 81 | 73 | 81 |
| Systematic thermal instability ($T_i$) | 4.76 | 2.03 | 2.45 |
| Calculated $T_m$, °C | **32** | **50** | **44** |
| Measured threshold $T_m$, °C* | **32** | **48** | **40** |
| References for measured $T_m$ | (9) | (9, 28) | (9) |

Note: * measured thresholds are based on the isolated hNBD1-Δ(RE, RI).

## FIGURES

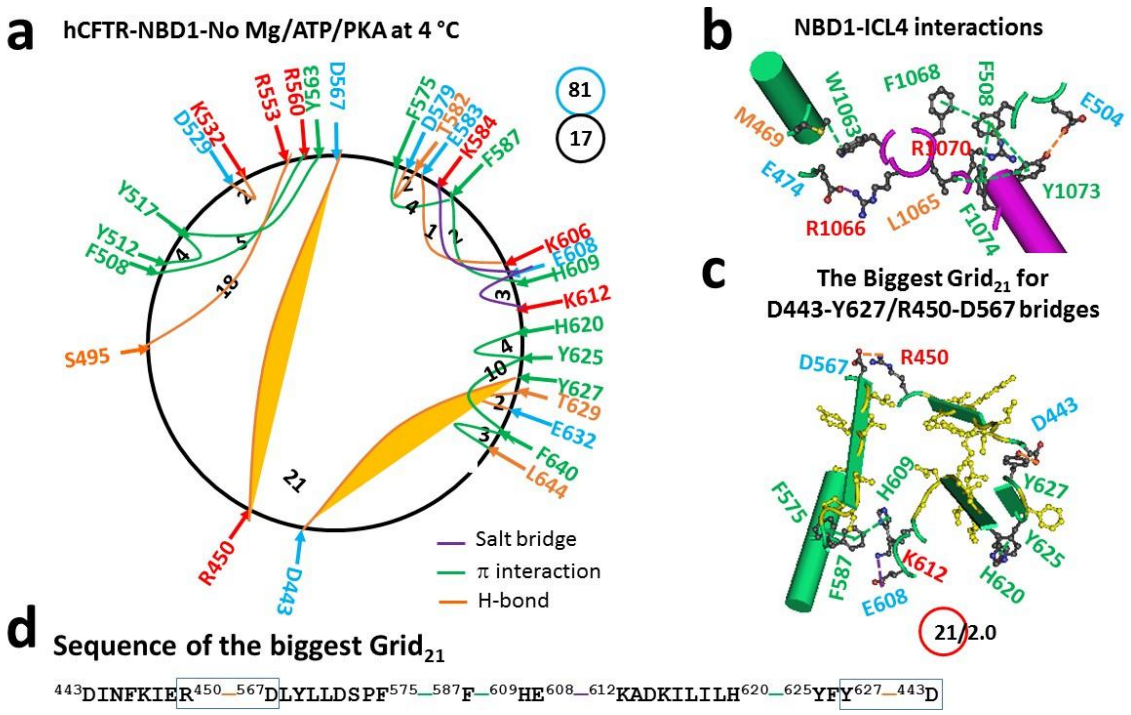


**Figure 1**. The thermoring structures of dephosphorylated hCFTR with F508 in the closed state at 4 °C. (**a**) The grid-like noncovalently interacting mesh network based on the cryo-EM structure of hCFTR with F508 in the absence of Mg/ATP/PKA at 4 °C (PDB ID, 5UAK, 3.87 Å). Salt bridges, H-bonds and π interactions are colored purple, orange, and green, respectively. The black numbers label the constrained grid sizes needed to control the least-stable noncovalent interactions in the grids. The least-stable D443-Y627 and R450-D567 H-bonds in the biggest $Grid_{21}$ are highlighted. The total grid sizes and the total grid size-controlled noncovalent interactions along the single polypeptide chain of NBD1 from E384 to M645 are shown in cyan and black circles, respectively. (**b**) Noncovalent interactions at the NBD1/ICL4 interface. (**c**) The structure of the biggest $Grid_{21}$ with a 21-residue size to control the least-stable D443-Y627 and R450-D567 H-bonds. The grid size and the equivalent basic H-bonds for the least-stable noncovalent interaction are shown in and near a red circle. (**d**) The sequence of the biggest $Grid_{21}$ to control the least-stable D443-Y627 and R450-D567 H-bonds in the blue box.

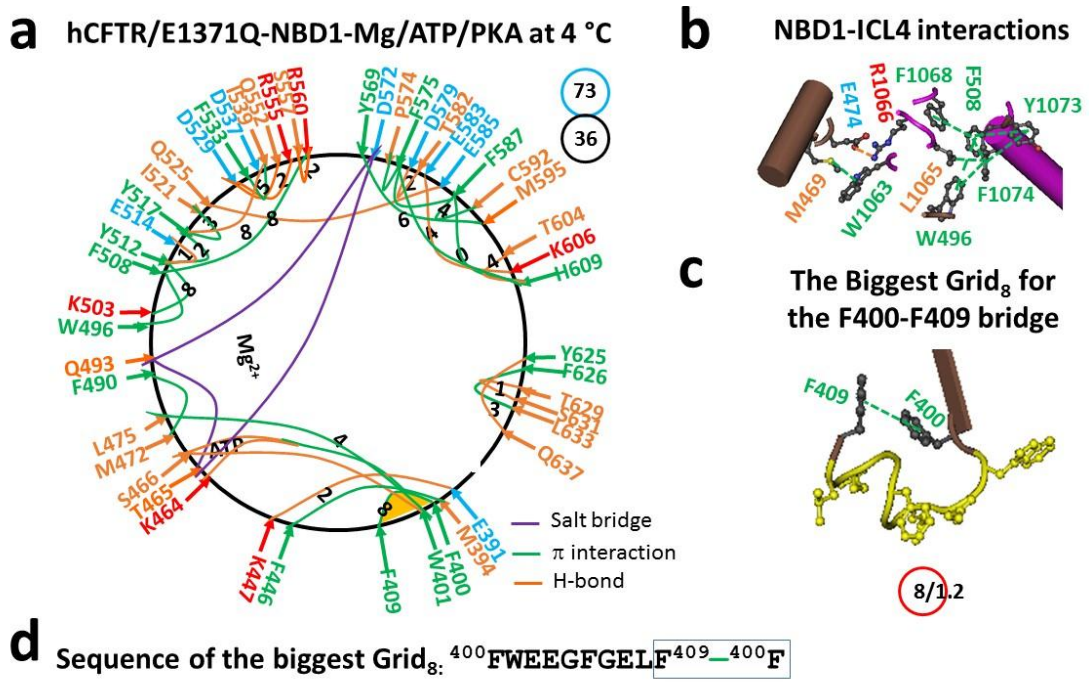


**Figure 2**. The thermoring structures of phosphorylated hCFTR/E1371Q with F508 in the open state at 4 °C. (**a**) The grid-like noncovalently interacting mesh network based on the cryo-EM structure of hCFTR/E1371Q with F508 in the presence of Mg/ATP/PKA at 4 °C (PDB ID, 6MSM, 3.2 Å). Salt bridges, H-bonds and π interactions are colored purple, orange, and green, respectively. The constrained grid sizes required to control the least-stable noncovalent interactions in the grids are labeled with black numbers. The least-stable F400-F409 π interaction in the biggest $Grid_8$ is highlighted. The total grid sizes and the total grid size-controlled noncovalent interactions along the single peptide chain of NBD1 from E384 to Q637 are shown in cyan and black circles, respectively. (**b**) Noncovalent interactions at the NBD1/ICL4 interface. (**c**) The structure of the biggest $Grid_8$ with an 8-residue size to control the least-stable F400-F409 π interaction. The grid size and the equivalent basic H-bonds for the least-stable noncovalent interaction are shown in and near a red circle. (**d**) The sequence of the biggest $Grid_8$ to control the least-stable F400-F409 π interaction in the blue box.

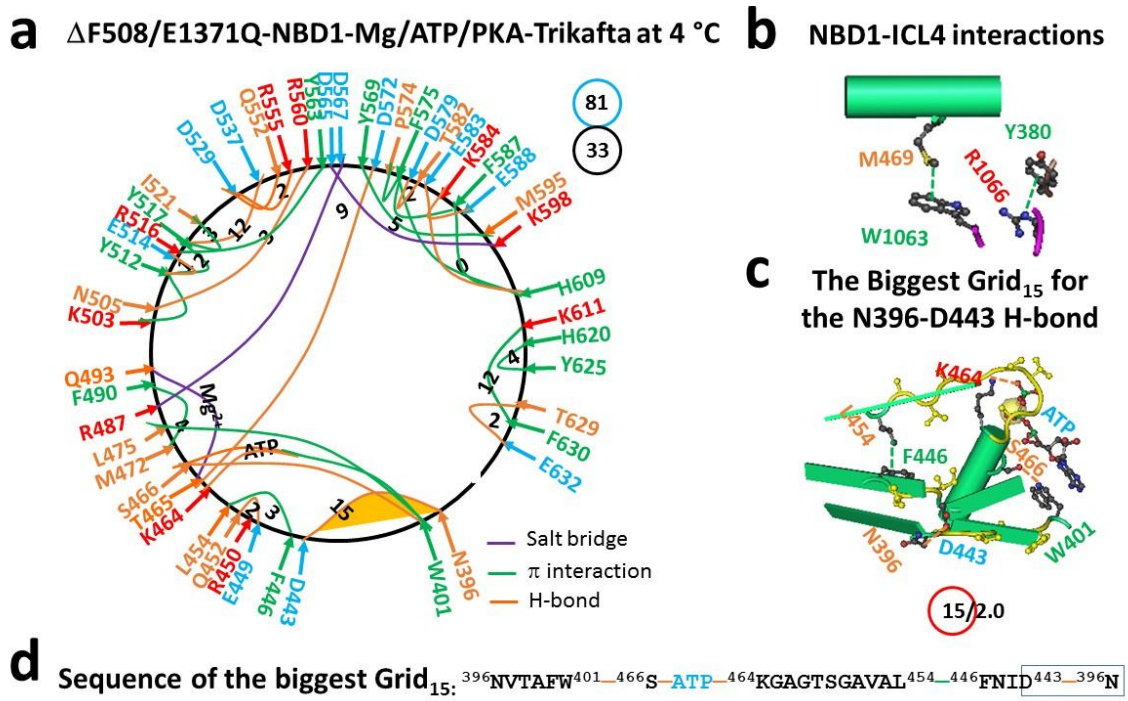


**Figure 3**. The thermoring structures of phosphorylated hCFTR/E1371Q/ΔF508 with Trikafta bound in the open state at 4 °C. (**a**) The grid-like noncovalently interacting mesh network based on the cryo-EM structure of hCFTR/E1371Q/ΔF508 with Trikafta bound in the presence of Mg/ATP/PKA at 4 °C (PDB ID, 8EIQ, 3.0 Å). Salt bridges, H-bonds and π interactions are colored purple, orange, and green, respectively. The constrained grid sizes required to control the least-stable noncovalent interactions in the grids are labeled with black numbers. The least-stable N396-D443 H-bond in the biggest $Grid_{15}$ is highlighted. The total grid sizes and the total grid size-controlled noncovalent interactions along the single peptide chain of NBD1 from L383 to L636 are shown in cyan and black circles, respectively. (**b**) Noncovalent interactions at the NBD1/ICL4 interface (Y380 is at the TMD1-NBD1 linker). (**c**) The structure of the biggest $Grid_{15}$ with a 15-residue size to control the least-stable N396-D443 H-bond. The grid size and the equivalent basic H-bonds for the least-stable noncovalent interaction are shown in and near a red circle. (**d**) The sequence of the biggest $Grid_{15}$ to control the least-stable N396-D443 H-bond in the blue box.

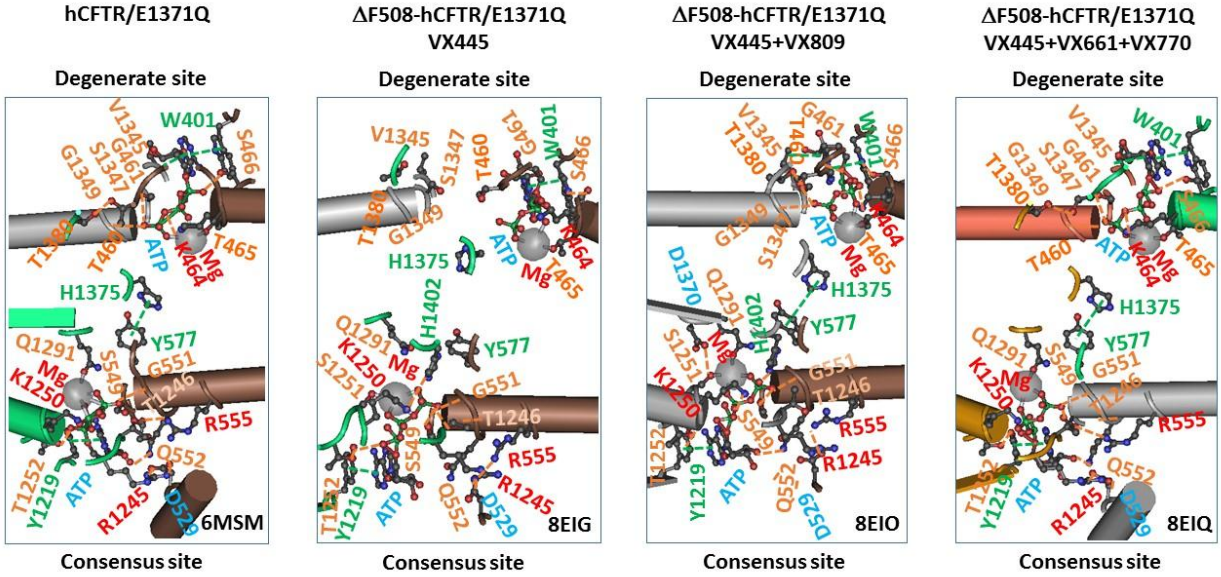


**Figure 4**. Mg/ATP-mediated NBD1-NBD2 interactions of hCFTR/E1371Q with or without F508- in response to modulators. The cryo-EM structures of CFTR constructs such as open phosphorylated hCFTR/E1371Q with Mg/ATP bound (PDB, 6MSM), open phosphorylated ΔF508-hCFTR-E1371Q with Mg/ATP/Trikafta bound (PDB, 8EIQ), open phosphorylated ΔF508-hCFTR-E1371Q with Mg/ATP/VX-445/VX-809 bound (PDB, 8EIO), closed phosphorylated ΔF508-hCFTR-E1371Q with Mg/ATP/VX-445 bound (PDB, 8EIG) are used for the models.

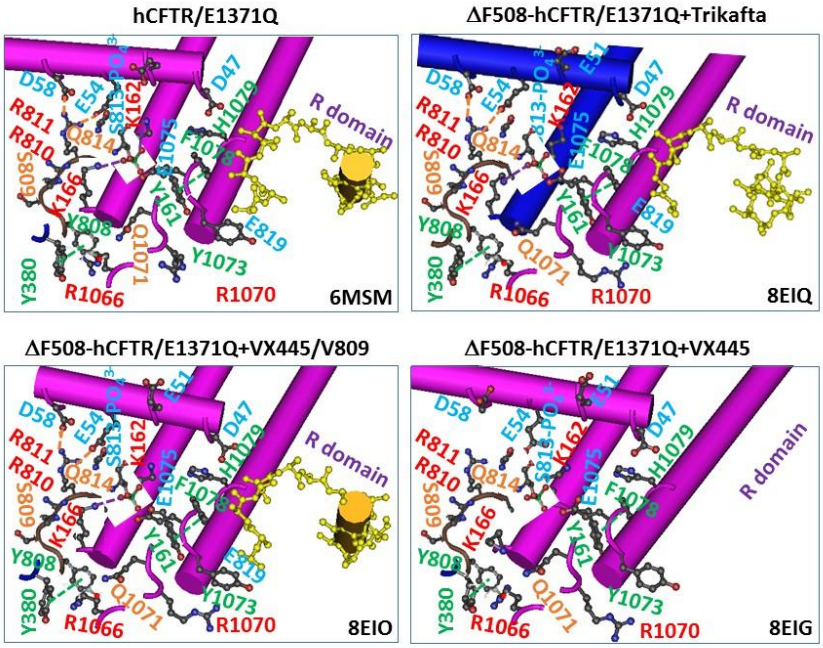


**Figure 5**. Specific interactions of the dynamic phosphorylated S813 site with ICL1/ICL4/NBD1 of -hCFTR/E1371Q with and without F508 in respons to modulators. The cryo-EM structures of CFTR constructs such as open phosphorylated hCFTR/E1371Q with Mg/ATP bound (PDB, 6MSM), open phosphorylated ΔF508-hCFTR-E1371Q with Mg/ATP/Trikafta bound (PDB, 8EIQ), open phosphorylated ΔF508-hCFTR-E1371Q with Mg/ATP/VX-445/VX-809 bound (PDB, 8EIO), closed phosphorylated ΔF508-hCFTR-E1371Q with Mg/ATP/VX-445 bound (PDB, 8EIG), and open phosphorylated hCFTR-E1371Q with Mg/ATP/PKA-C bound (PDB, 9DW9) are used for the models.

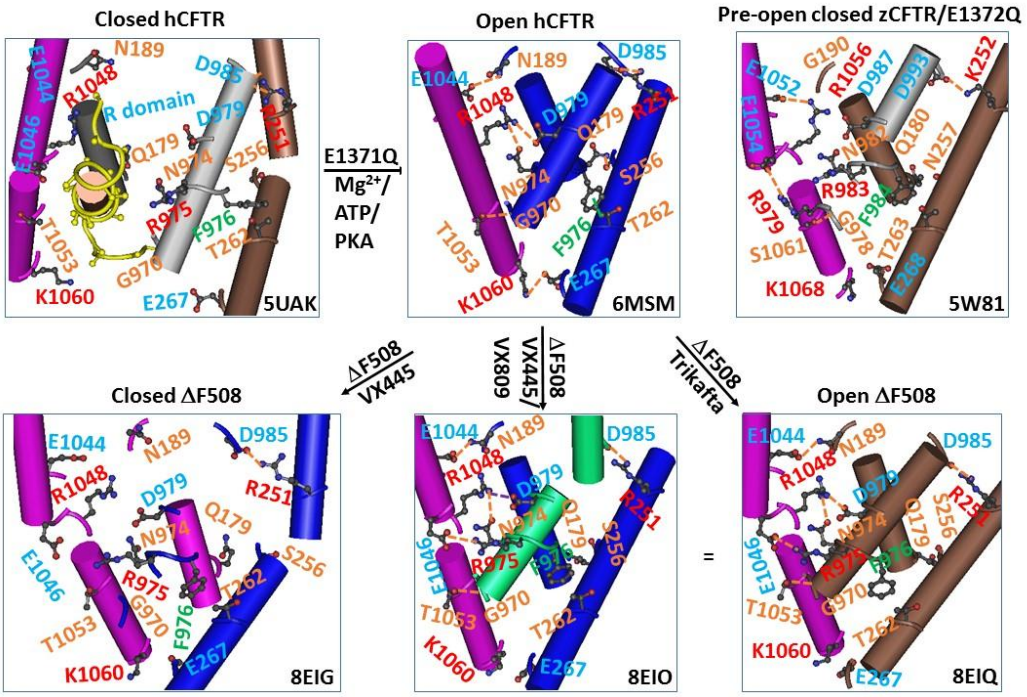


**Figure 6**. Phosphorylation-dependent cytoplasmic TMD1-TMD2 interactions of hCFTR/E1371Q with or without F508 in repsonse to modulators. Closed and open hCFTR and pre-open closed zCFTR are controls. The cryo-EM structures of CFTR constructs such as closed dephosphorylated hCFTR (PDB, 5UAK), open phosphorylated hCFTR-E1371Q with Mg/ATP bound (PDB, 6MSM), pre-open closed phosphorylated zCFTR-E1372Q with Mg/ATP bound (PDB, 5W81), open phosphorylated ΔF508-hCFTR-E1371Q with Mg/ATP/Trikafta bound (PDB, 8EIQ), open phosphorylated ΔF508-hCFTR-E1371Q with Mg/ATP/VX-445/VX-809 bound (PDB, 8EIO) and closed phosphorylated ΔF508-hCFTR-E1371Q with Mg/ATP/VX-445 bound (PDB, 8EIG) are used for the models.

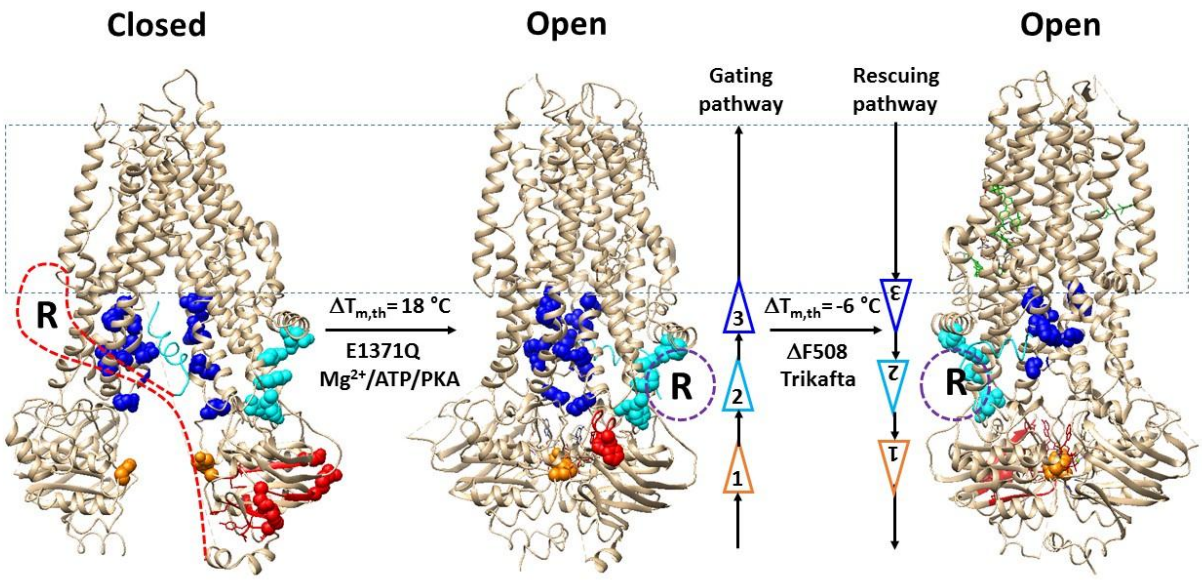


**Figure 7.** Putative pathway for Trikafta to correct the primary gating and subsequent thermal defects of ΔF508-CFTR. Cryo-EM structures of closed dephosphorylated hCFTR (PDB: 5UAK), open phosphorylated hCFTR/E1371Q with Mg/ATP bound (PDB: 6MSM) and open phosphorylated hCFTR/ΔF508/E1371Q with Mg/ATP/Trikafta bound (PDB: 8EIQ) are used for the models. The red curves and the purple circles represent the dephosphorylated and phosphorylated R domain, respectively. The critical residues for cytoplasmic TMD1-TMD2 interactions are colored blue. The C-terminal region of the R domain and S813-binding sites are colored in cyan. The residues for the NBD dimerization hallmark, the Y577-H1375 π bridge, are colored in orange. Three modulators such as VX-445, VX-661 andVX-770 are colored green and the biggest thermorings in NBD1 are shown in red. The residues responsible for the least-stable noncovalent interactions in NBD1 are shown in space fills. Three key interdomain interactions are shown as triangles.